



Cite this: *Chem. Commun.*, 2021, 57, 7954

Received 19th May 2021,
Accepted 9th July 2021

DOI: 10.1039/d1cc02629a

rsc.li/chemcomm

A metal–organic cage-based nanoagent for enhanced photodynamic antitumor therapy†

Wen-Yan Li,^{‡a} Chao-Wei Zhao,^{‡b} Yue-Feng Zhang,^b Qun Guan,^{id a} Jing-Jing Wan,^a Jian-Ping Ma,^{id a} Yan-An Li^{id *a} and Yu-Bin Dong^{id *a}

Herein, we report, for the first time, a $\text{Pd}_6\text{L}_8(\text{NO}_3)_{5.4}(\text{ICG})_{6.6}$ (ICG = indocyanine green) cage-based hexagonal nanoplate (**3**) via a combined nanoprecipitation and solid-state anion-exchange approach. Nanoplate **3** possesses enhanced near-infrared (NIR) light-triggered $^1\text{O}_2$ generation, high cellular uptake selective lysosome-targeting ability, and, consequently, excellent antineoplastic activity.

Metal–organic complexes (MOCs),^{1–4} which are assembled from metal ions and convergent organic ligands, represent a tantalizing class of discrete metal–organic species due to their well-defined metallacycle- and metallacage-structures and their wide applications. Compared with catalysis,^{5,6} molecular recognition,⁷ and sensing,⁸ their applications in biomedicine have drawn much less attention.⁹ For example, only a handful of MOC photosensitizers, which are all generated from photosensitive organic ligands, have been reported for antitumor phototherapy so far.^{10–16} This might be a result of their inherent hydrophobicity,¹⁷ severe aggregation, low cell permeability, and difficulty in constructing MOCs using organic ligands with a specific geometry, hydrophilicity, and photosensitivity.

Recently, self-assembly-derived nanomaterials with regular geometric shapes have received intense attention in biomedical applications, especially in antitumor treatment. For example, Lin and co-workers reported nanoscale metal–organic framework (MOF)-based hexagonal plates for efficient photodynamic antitumor therapy (PDT).^{18,19} We recently reported COF-based

nanoballs which exhibited an enhanced antitumor efficiency via PDT/ Ca^{2+} -overload and PDT/PTT synergistic therapy.^{20,21} Inspired by this, we speculate that MOC-nanocrystallization could also lead to MOC-nanoparticles with regular geometry, which would allow their endocytosis-based cellular uptake to be significantly improved, and consequently, augment their therapeutic efficacy. On the other hand, MOCs are usually electro-positive, and we envision that their existing counter anions could in principle be exchanged with some photoactive anionic organic dyes. In this way, the nanocrystallization of organic photosensitizers could be realized, and enhanced phototherapy, such as antitumor PDT, could be achieved in their own right.

Among various MOCs, M_6L_8 -type molecular spheres with an octahedral geometry remain quite rare. We have previously reported a $\text{Pd}_6\text{L}_8(\text{NO}_3)_{12}$ assembly (**1**, $\text{L} = 1,3,5$ -tris(4'-pyridyloxadiazone)-2,4,6-triethylbenzene) (Fig. 1), which was then assumed to be a ball-like nanocage, and which was determined by MS and NMR measurements.²² Unceasing endeavors allowed us eventually to obtain its

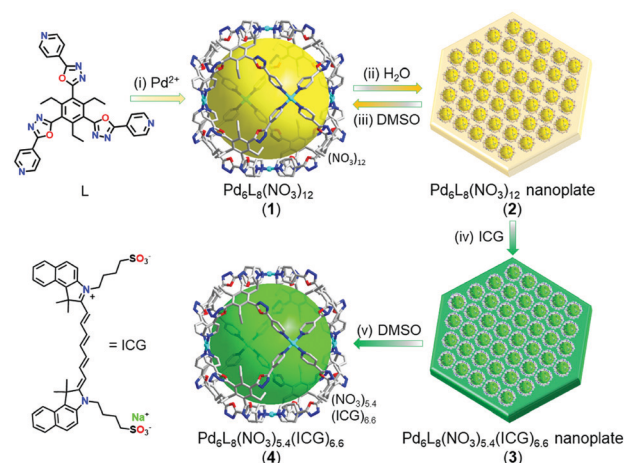


Fig. 1 Synthesis of **1–4**. The single-crystal structure of **1** (CCDC† 1840207) is shown (solvents and disordered anions are omitted for clarity). (i) $\text{Pd}(\text{NO}_3)_2$, $\text{DMSO}-d_6$, 70 °C, and 2 h; (ii) H_2O , 25 °C, and 4 h; (iii) DMSO and 25 °C; (iv) ICG, H_2O , 25 °C, and 24 h; and (v) DMSO and 25 °C.

^a College of Chemistry, Chemical Engineering and Materials Science, Collaborative Innovation Center of Functionalized Probes for Chemical Imaging in Universities of Shandong, Key Laboratory of Molecular and Nano Probes, Ministry of Education, Shandong Normal University, Jinan 250014, P. R. China. E-mail: yanani@sdnu.edu.cn, yubindong@sdnu.edu.cn

^b Institute of Applied Chemistry, Jiangxi Academy of Sciences, Nanchang 330096, P. R. China

† Electronic supplementary information (ESI) available: Materials and methods, synthetic procedures, experimental details, supplementary figures and table. CCDC 1840207. For ESI and crystallographic data in CIF or other electronic format see DOI: 10.1039/d1cc02629a

‡ These authors contributed equally to this work.

single-crystal structure (Table S1, ESI[†]), which is exactly consistent with our previous speculation. X-Ray single-crystal analysis revealed that **1** crystallizes in the tetragonal space group *I4/m*. The asymmetric unit has one L in a general position, one NO₃[−] on a mirror plane with 1/2-occupancy, and two Pd atoms (Pd1 with 1/2-occupancy at a site with *m*-symmetry and Pd2 with 1/4-occupancy at a site with four-fold symmetry). This corresponds with the formula Pd₆L₈(NO₃)₄; the contributions of some other species including NO₃[−] and some DMSO, CH₃CN and H₂O molecules of solvation were removed from the structure by the use of SQUEEZE. As shown in Fig. 1, the assembly of eight tridentate C₃-symmetric ligands L and six square-like D₄-symmetric Pd(II) nodes resulted in a spherical Pd-cage (**1**) with 12 open windows of ca. 13 × 11 Å. The ball diameter is ca. 28 Å, determined by the furthest opposite atom distance. The internal cavity volume is estimated to be ca. 4000 Å³. However, **1** is hydrophobic, which largely limits its use under physiological conditions.

Interestingly, when the DMSO solution of **1** was mixed with water in the ratio of 3:2 (v:v), **1** readily assembled into the nanoparticles of **2** (Fig. 2). Transmission electron microscopy (TEM) and atomic force microscopy (AFM) showed that the nanoparticles of **2** were obtained as regular hexagonal nanoplates with a size of ~160 nm and a thickness of ~20 nm (Fig. 2a, and Fig. S1a, ESI[†]). Furthermore, the hexagonal nanoplate **2** can be dissolved in DMSO as individual cages, which was evidenced by MS analysis (Fig. S1b, ESI[†]).

In order to fabricate MOC-based nanophotosensitizers, the photoactive anionic dye of indocyanine green (ICG) was selected to displace the uncoordinated NO₃[−] counterions in **2** via solid-state anion-exchange. To our delight, by simply immersing the nanoplates of **2** in an aqueous solution of ICG (molar ratio, ICG/nitrate = 1.7:1), the anion-exchange reaction occurred smoothly along with a naked-eye-detectable color change from light yellow to green (Fig. 2a and b, insets). After 24 h, the anion-exchange reaction reached an equilibrium, and

~55% of nitrates in **2** were replaced by ICG to afford **3** based on standard curves analysis (Fig. S2, ESI[†]). Of note, when **3** was dissolved in DMSO, a discrete molecular Pd₆L₈(NO₃)_{5.4}(ICG)_{6.6} cage of **4** was generated. Electrospray ionization mass spectrometry (ESI-MS) provided substantial evidence for the formation of Pd₆L₈(NO₃)_{5.4}(ICG)_{6.6}. Peaks at 1193.9640 (calcd 1193.9549), 1308.8544 (calcd 1308.8382), 1445.1548 (calcd 1445.1449), and 1582.9686 (calcd 1583.0049) corresponding to the fragments [Pd₆L₈(NO₃)₄(ICG)₂]⁶⁺, [Pd₆L₈(NO₃)₃(ICG)₃]⁶⁺, [Pd₆L₈(NO₃)₅(ICG)₂]⁵⁺, and [Pd₆L₈(NO₃)₄(ICG)₃]⁵⁺, respectively, for **4** were observed (Fig. S3a, ESI[†]), which are in good agreement with their calculated theoretical distributions. In addition, both Pd₆L₈ and ICG were detected in the ¹H NMR spectrum (Fig. S3b, ESI[†]), which further supported the formation of Pd₆L₈(NO₃)_{5.4}(ICG)_{6.6}.

By nanoprecipitation, together with solid-state anion-exchange, we successfully realized the nanocrystallization of MOCs and organic photosensitizers, which has laid down a solid foundation for their application in antitumor PDT. TEM indicated that the hexagonal shape of **2** was intact upon anion-exchange, suggesting that the anion-exchange process did not change its morphology (Fig. 2b). Dynamic light scattering (DLS) measurements revealed that the diameters of **2** and **3** were centered at 169.5 ± 20.6 nm and 178.3 ± 21.8 nm, respectively (Fig. 2c). It is expected that the slight size increase results from the large-sized ICG anions involved. In addition, the zeta potential increased from 36.6 ± 0.5 mV in **2** to 40.7 ± 0.8 mV in **3** after anion-exchange (Fig. S4, ESI[†]). As is known, the positive zeta potential can significantly enhance the interaction between the NPs and the negatively charged cancer cell membrane, consequently greatly promoting their endocytosis.²¹

In addition, we evaluated the stability of **3** in different physiological media (water, phosphate-buffered saline, and the cell culture medium of DMEM with 10% fetal bovine serum). Visual images of the samples after 72 h showed that **3** was well dispersed without any aggregation in all the selected media (Fig. S5, ESI[†]), indicating its high stability in different physiological media. DLS measurements also showed that **2** and **3** could be stably stored in the culture medium with the serum for 3 days (Fig. S6, ESI[†]).

As mentioned above, a significant color change occurred during the anion-exchange process. Ultraviolet-visible (UV-vis) absorption spectroscopy (Fig. 2d) revealed that no characteristic absorbance above 400 nm was observed for **2**, while **3** had a maximum absorption at ~820 nm in the NIR region. Compared with the ICG absorption (~779 nm), **3** was obviously red-shifted, implying a strong interaction between the ICG anion and the Pd-cage.²³ However, from the simple mixing of ICG with **2**, the UV absorption of this mixture was similar to that of free ICG, see Fig. S7 (ESI[†]).

Based on the NIR absorption displayed by **3**, an 808 nm laser was used as the excitation light source to test its photodynamic performance in which 1,3-diphenylisobenzofuran (DPBF) was used as the ¹O₂ probe.²⁴ As shown in Fig. 3a, DPBF exhibited a continuous decrease in absorbance intensity at 414 nm, which decreased to 6% when **3** (10 μg mL^{−1}) was exposed to an 808 nm laser (100 mW cm^{−2}) for 5 min in EtOH, suggesting

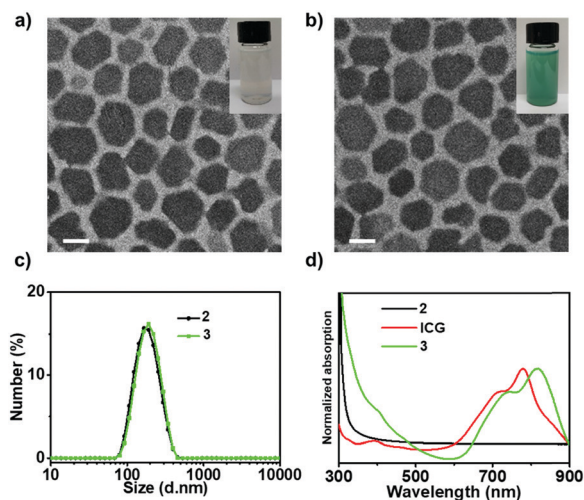


Fig. 2 (a and b) TEM images of **2** and **3** and their corresponding images of the PBS suspensions (inset); scale bar, 100 nm. (c) DLS size profiles of **2** and **3** in PBS at 25 °C. (d) UV-vis absorption spectra of **2**, ICG and **3**.

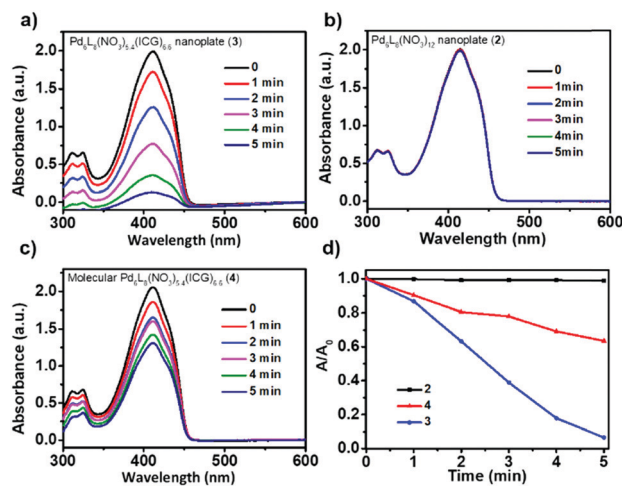


Fig. 3 Photodynamic properties of **3** (a), **2** (b) and **4** (c). (d) Comparison of the decay rate of DPBF induced by **2**, **3** and **4**.

highly efficient $^1\text{O}_2$ generation. In control groups, DPBF showed a negligible absorbance change in the presence of **2** (Fig. 3b) and a much lower $^1\text{O}_2$ generation efficiency in the presence of **4** (down to 64% in 5 min, Fig. 3c) under the same conditions. The behaviour of **4** is different from **3**, and TEM showed that the discrete molecular cage of **4** promptly aggregated into large-sized vesicles in the test system (Fig. S8, ESI†). Compared with **2** and **4**, **3** is more suitable for antitumor treatment by PDT (Fig. 3d).

Encouraged by the excellent stability and high $^1\text{O}_2$ generation efficiency of **3**, we then examined its *in vitro* antitumor ability against MCF-7 cells (the human breast adenocarcinoma cell line). After incubation with **3** for 2 h, the cultured MCF-7 cells displayed strong fluorescence under a confocal laser scanning microscope (CLSM) (Fig. 4a), indicating that **3** possessed a high cell permeability. By contrast, **4** exhibited a much lower cellular uptake than that of **3** (Fig. 4a), indicating that **4** was not suitable for use as an antitumor agent. After the MCF-7 cells were incubated with **3** and stained with Lyso Tracker Green or Mito Tracker Green FM,²⁵ CLSM imaging showed that **3** was mainly colocalized with lysosomes after 4 h (Fig. S9, ESI†).

Next, the cell proliferation and cytotoxicity were quantitatively assessed *via* the Cell Counting Kit-8 (CCK-8) cell viability assay.²⁰ Without laser irradiation, no apparent cytotoxic effect was observed in MCF-7 cells, even at a concentration as high as $500\ \mu\text{g mL}^{-1}$ (Fig. S10, ESI†), indicating that **3** possessed excellent biocompatibility. In addition, **3** displayed an excellent intracellular $^1\text{O}_2$ generation ability, which was well demonstrated by CLSM in the presence of the specific Singlet Oxygen Sensor Green (SOSG) probe.^{18,19,24} As is shown, negligible fluorescence was observed when the cells were in PBS or with **3** ($10\ \mu\text{g mL}^{-1}$) in the dark. Under light irradiation, the **3** ($10\ \mu\text{g mL}^{-1}$)-treated MCF-7 cell group, however, displayed strong green fluorescence after 5 min, suggesting that a large amount of $^1\text{O}_2$ was generated (Fig. S11, ESI†). Excess $^1\text{O}_2$ usually leads to lysosomal membrane permeabilization (LMP), which can result in the release of lysosomal proteases,²⁶ where they induce apoptotic signaling. As shown in Fig. 4b, after 8 min of laser irradiation, the

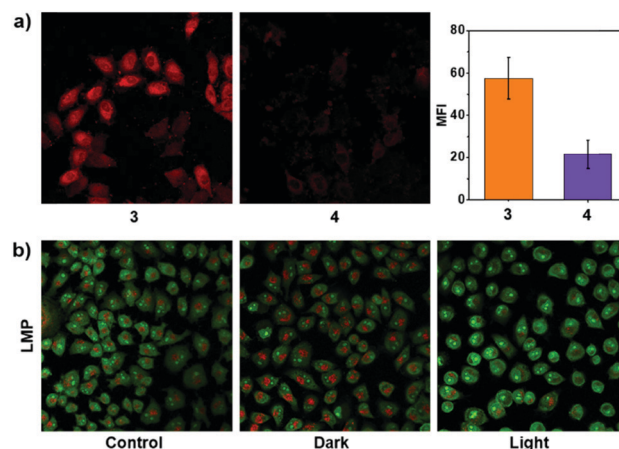


Fig. 4 Confocal laser scanning microscope images. (a) Fluorescence images of MCF-7 cells incubated with **3** and **4**. The cellular uptake was reflected by the mean fluorescence intensity (MFI) of red fluorescence. Data are presented as the mean \pm SD ($n = 5$). (b) Detection of **3**-based lysosomal membrane permeability using acridine orange (AO).

red fluorescence within the cells was significantly decreased, while the green emission of acridine orange (AO) in the cytosol and nucleus increased, which implied that **3** triggered $^1\text{O}_2$ generation to effectively promote cell death *via* the lysosome-associated pathway.²⁷

For *in vitro* experiments, **3** with a concentration ranging from 0 to $30\ \mu\text{g mL}^{-1}$ was added into a 96-well plate and incubated with MCF-7 cells. After 2 h, the MCF-7 cells were irradiated by an 808 nm laser for 8 min, and the cell viabilities were significantly decreased. As shown in Fig. 5a, when the concentration of **3** was $30\ \mu\text{g mL}^{-1}$, the cell viability decreased sharply to $21.4 \pm 2.4\%$, whereas when incubating with the same concentration of **4** the cell viability decreased to only $59.2 \pm 2.2\%$ (Fig. S12, ESI†). This observation was very consistent with the high cellular uptake and enhanced $^1\text{O}_2$ generation of **3** described above.

Before the *in vivo* experiments, the hemocompatibility of **3** was also evaluated for safety.²⁸ The hemolysis ratios of the red blood corpuscles at a concentration of **3** of $200\ \mu\text{g mL}^{-1}$ were negligible (percent hemolysis $< 2\%$) compared with the positive control group (Fig. S13, ESI†), which confirmed its good hemocompatibility. To evaluate the therapeutic efficacy of **3** *in vivo*, experiments were conducted on the MCF-7 xenograft model of nude mice. Once the average tumor volume had reached $\sim 100\ \text{mm}^3$, the tumor-bearing mice ($n = 25$) were randomly divided into five groups: (i) Dulbecco's phosphate-buffered saline (DPBS)-treated group (control group), (ii) **2** ($100\ \mu\text{L}$, $100\ \mu\text{g mL}^{-1}$, 8 min) with 808 nm ($100\ \text{mW cm}^{-2}$) laser irradiation, (iii) ICG ($100\ \mu\text{L}$, $47\ \mu\text{g mL}^{-1}$, 8 min) with 808 nm ($100\ \text{mW cm}^{-2}$) laser irradiation, (iv) **3** ($100\ \mu\text{L}$, $100\ \mu\text{g mL}^{-1}$, 8 min) in the dark and (v) **3** ($100\ \mu\text{L}$, $100\ \mu\text{g mL}^{-1}$, 8 min) with 808 nm ($100\ \text{mW cm}^{-2}$) laser irradiation. Groups (ii), (iii), and (v) were irradiated using a laser at 4 h after the intratumor injection. The tumor volume and weight were recorded every two days after the initial treatment for 15 days. As presented in Fig. 5b, the tumors in groups (i)–(iv) grew quickly, suggesting

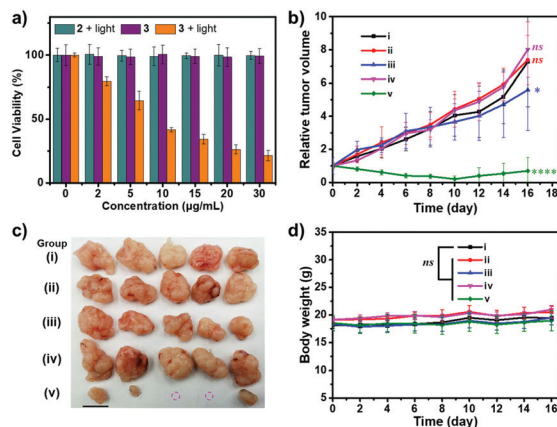


Fig. 5 (a) Antitumor therapy *in vitro*. Viability of MCF-7 cells treated with **2** or **3** plus 808 nm laser irradiation (100 mW cm^{-2} , 8 min). (b) Tumor volume of nude mice in various groups during the treatment. (i) DPBS-treated group, (ii) **2** with 808 nm laser irradiation, (iii) ICG with 808 nm laser irradiation, (iv) **3** and (v) **3** with 808 nm laser irradiation (100 mW cm^{-2}). (c) Images of the excised tumor tissues in various groups after treatment. Scale bar, 1 cm. (d) Body weight of the mice in various groups during the treatment. Data are presented as the mean \pm SD ($n = 5$). **** $p < 0.0001$, * $p < 0.05$; ns, no significance ($p > 0.05$).

that the **2** + light, ICG + light, and **3** alone groups had no effect on inhibiting tumor growth, while tumors in **3** + light group showed negative growth. Of note, some tumors in group (v) were completely eradicated by **3** under light irradiation, while the sizes of the other tumors were significantly reduced from ~ 150 to $\sim 20 \text{ mm}^3$ (Fig. 5c). Thermal imaging showed that the temperature barely increased during the photodynamic therapy (Fig. S14, ESI[†]). In addition, after the PDT with **3** under light irradiation, no notable side effects were observed, which was well illustrated by the mice body weight analysis (Fig. 5d) and the histology analysis of their major organs collected after treatment (Fig. S15, ESI[†]). Tissue fluorescence imaging showed that ICG-containing **3** was mainly located at the tumor site after the injection and did not spread to other tissues in 24 h (Fig. S16, ESI[†]).

In conclusion, we report a MOC-based photoactive antitumor nanoagent *via* a facile nanoprecipitation–anion-exchange coalescent approach. The obtained ICG-involved MOC-nanoplates are very stable under physiological conditions and possess enhanced NIR light-induced $^1\text{O}_2$ generation, high cellular uptake, and selective lysosome-targeting ability, which allows them to be a highly active antitumor photosensitizer *via* PDT. Compared with reports on organic ligand-derived phototherapy, the photoactive counter anion-triggered antitumor phototherapy on MOCs is unprecedented. We believe that our approach is general and viable for the fabrication of many other types of MOC-based nanomedicines for a variety of tumor treatments with both high efficiency and selectivity.

The authors acknowledge financial support from the National Natural Science Foundation of China (21971153, 21805172, and 21801213), the Major Basic Research Projects

of Shandong Provincial Natural Science Foundation (No. ZR2020ZD32), and the Taishan Scholars Climbing Program of Shandong Province.

Conflicts of interest

There are no conflicts to declare.

Notes and references

- S. Leininger, B. Olenyuk and P. J. Stang, *Chem. Rev.*, 2000, **100**, 853–908.
- M. Fujita, M. Tominaga, A. Hori and B. Therrien, *Acc. Chem. Res.*, 2005, **38**, 369–378.
- J. R. Nitschke, *Acc. Chem. Res.*, 2007, **40**, 103–112.
- A. J. Gosselin, C. A. Rowland and E. D. Bloch, *Chem. Rev.*, 2020, **120**, 8987–9014.
- C. J. Brown, F. D. Toste, R. G. Bergman and K. N. Raymond, *Chem. Rev.*, 2015, **115**, 3012–3035.
- Y. Fang, J. A. Powell, E. Li, Q. Wang, Z. Perry, A. Kirchon, X. Yang, Z. Xiao, C. Zhu, L. Zhang, F. Huang and H.-C. Zhou, *Chem. Soc. Rev.*, 2019, **48**, 4707–4730.
- A. Galan and P. Ballester, *Chem. Soc. Rev.*, 2016, **45**, 1720–1737.
- M. Pan, W.-M. Liao, S.-Y. Yin, S.-S. Sun and C.-Y. Su, *Chem. Rev.*, 2018, **118**, 8889–8935.
- N. Ahmad, H. A. Younus, A. H. Chughtai and F. Verpoort, *Chem. Soc. Rev.*, 2015, **44**, 9–25.
- M. G. Walker, P. J. Jarman, M. R. Gill, X. Tian, H. Ahmad, P. A. N. Reddy, L. McKenzie, J. A. Weinstein, A. J. H. M. Meijer, G. Battaglia, C. G. W. Smythe and J. A. Thomas, *Chem. – Eur. J.*, 2016, **22**, 5996–6000.
- Z. Zhou, J. Liu, T. W. Rees, H. Wang, X. Li, H. Chao and P. J. Stang, *Proc. Natl. Acad. Sci. U. S. A.*, 2018, **115**, 5664–5669.
- Y. Yao, R. Zhao, Y. Shi, Y. Cai, J. Chen, S. Sun, W. Zhang and R. Tang, *Chem. Commun.*, 2018, **54**, 8068–8071.
- J. Zhou, Y. Zhang, G. Yu, M. R. Crawley, C. R. P. Fulong, A. E. Friedman, S. Sengupta, J. Sun, Q. Li, F. Huang and T. R. Cook, *J. Am. Chem. Soc.*, 2018, **140**, 7730–7736.
- G. Gupta, A. Das, K. C. Park, A. Tron, H. Kim, J. Mun, N. Mandal, K.-W. Chi and C. Y. Lee, *Inorg. Chem.*, 2017, **56**, 4615–4621.
- G. Yu, S. Yu, M. L. Saha, J. Zhou, T. R. Cook, B. C. Yung, J. Chen, Z. Mao, F. Zhang, Z. Zhou, Y. Liu, L. Shao, S. Wang, C. Gao, F. Huang, P. J. Stang and X. Chen, *Nat. Commun.*, 2018, **9**, 4335.
- H. Sepehrpour, W. Fu, Y. Sun and P. J. Stang, *J. Am. Chem. Soc.*, 2019, **141**, 14005–14020.
- E. G. Percástegui, T. K. Ronson and J. R. Nitschke, *Chem. Rev.*, 2020, **120**, 13480–13544.
- K. Lu, C. He and W. Lin, *J. Am. Chem. Soc.*, 2015, **137**, 7600–7603.
- C. He, K. Lu, D. Liu and W. Lin, *J. Am. Chem. Soc.*, 2014, **136**, 5181–5184.
- Q. Guan, L. Zhou, F. Lv, W. Li, Y. Li and Y. Dong, *Angew. Chem., Int. Ed.*, 2020, **59**, 18042–18047.
- Q. Guan, L.-L. Zhou, Y.-A. Li, W.-Y. Li, S. Wang, C. Song and Y.-B. Dong, *ACS Nano*, 2019, **13**, 13304–13316.
- C.-W. Zhao, J.-P. Ma, Q.-K. Liu, Y. Yu, P. Wang, Y.-A. Li, K. Wang and Y.-B. Dong, *Green Chem.*, 2013, **15**, 3150–3154.
- S. Gan, X. Tong, Y. Zhang, J. Wu, Y. Hu and A. Yuan, *Adv. Funct. Mater.*, 2019, **29**, 1902757.
- Q. Guan, L.-L. Zhou, Y.-A. Li and Y.-B. Dong, *Inorg. Chem.*, 2018, **57**, 10137–10145.
- Q. Guan, D.-D. Fu, Y.-A. Li, X.-M. Kong, Z.-Y. Wei, W.-Y. Li, S.-J. Zhang and Y.-B. Dong, *iScience*, 2019, **14**, 180–198.
- R. Han, M. Zhao, Z. Wang, H. Liu, S. Zhu, L. Huang, Y. Wang, L. Wang, Y. Hong, Y. Sha and Y. Jiang, *ACS Nano*, 2020, **14**, 9532–9544.
- M. Chen, X. Liang, C. Gao, R. Zhao, N. Zhang, S. Wang, W. Chen, B. Zhao, J. Wang and Z. Dai, *ACS Nano*, 2018, **12**, 7312–7326.
- X. Qian, Z. Gu and Y. Chen, *Mater. Horiz.*, 2017, **4**, 800–816.